BIOCHEMISTRY

F-actin disassembly factor MICAL1 binding to Myosin Va mediates cargo unloading during cytokinesis

Fengfeng Niu[1,2]*, Kang Sun[1,3]*, Wenjie Wei[1,4], Cong Yu[1,3]†, Zhiyi Wei[1,2]†

Motor-mediated intracellular trafficking requires motors to position cargoes at proper locations. Myosin Va (MyoVa), an actin-based motor, is a classic model for studying cargo transport. However, the molecular basis underlying cargo unloading in MyoVa-mediated transport has remained enigmatic. We have identified MICAL1, an F-actin disassembly regulator, as a binding partner of MyoVa and shown that MICAL1-MyoVa interaction is critical for localization of MyoVa at the midbody. By binding to MICAL1, MyoVa-mediated transport is terminated, resulting in vesicle unloading at the midbody for efficient cytokinesis. The MyoVa/MICAL1 complex structure reveals that MICAL1 and F-actin assembly factors, Spires, share an overlapped binding surface on MyoVa, suggesting a regulatory role of F-actin dynamics in cargo unloading. Down-regulating F-actin disassembly by a MICAL1 mutant significantly reduces MyoVa and vesicles accumulating at the midbody. Collectively, our findings demonstrate that MyoVa binds to MICAL1 at the midbody destination and triggers F-actin disassembly to unload the vesicle cargo.

INTRODUCTION

Intracellular cargo transport is fundamental for a broad range of cellular activities (*1–3*), especially for the processes involving extensive and rapid rearrangements of cellular components, such as cell division and neuromodulation (*3–5*). In these processes, molecular motors (e.g., myosins, kinesins, and dyneins) transport various intracellular materials along cytoskeletal filaments (e.g., actin filaments and microtubules). Cargo loading and unloading at the right positions and moments require molecular motors to be spatially and temporally regulated during the entire transport process (*6–10*). The incorrect positioning of cargoes caused by motor malfunction during cargo transport can induce severe diseases, such as various neurological diseases (*11–13*).

As actin-based motors, unconventional class V myosins are critical in transporting a diverse array of intracellular cargoes, including different types of organelles, vesicles, protein complexes, and mRNAs, thus participating in a number of cellular processes and essential for cell functions (*14–16*). In vertebrates, class V myosins include three members: MyoVa, MyoVb, and MyoVc (*14*). Among them, MyoVa is a classic model for studying intracellular cargo transport, e.g., pigment granule transport in melanocytes (*17*) and neuronal vesicle transport in neurons (*18*). Defective mutations in MyoVa lead to "dilute-lethal" in mice (*19*) and Griscelli syndrome in human (*20*). MyoVa contains an adenosine triphosphatase (ATPase) motor domain at the N terminus to associate with F-actin and generate force and a globular tail domain (GTD) at the C terminus to associate with cargoes (Fig. 1A) (*21*). Despite the fact that MyoVa has been extensively characterized regarding its motor properties and cargo recognition mechanisms (*15*, *22*, *23*), the molecular basis underlying the cargo unloading in the MyoVa-mediated transport remains elusive.

Because of its dynamic nature, F-actin as tracks for myosin motors is considered to play regulatory roles in the MyoVa-mediated cargo transport (*13*, *24*, *25*). An in vitro study showed that the MyoVa-mediated liposome transport was influenced by different arrangements of three-dimensional actin networks, including different F-actin density, position, and polarity (*26*). Drug-induced suppression of F-actin dynamics in cells inhibited the MyoVa-mediated transports of pigment granules and lysosomes (*25*). Recently, Spire proteins, important for actin nucleation and polymerization, were reported to regulate actin-based vesicle transport by directly interacting with MyoVa (*27*, *28*).

Here, we identified molecule interacting with CasL 1 (MICAL1), an actin oxidase in promoting F-actin disassembly (*29*, *30*), as a previously unknown binding partner of MyoVa. By binding to a 23-residue fragment in MICAL1, MyoVa is docked at either one side or both sides of the midbody, which is a subcellular structure required for cytokinesis (*31*). As MyoVa's cargoes, Rab11a-positive vesicles have been suggested to supply essential membrane and protein components to midbody for successful abscission during cytokinesis (*32–34*). Our cellular data indicate that Rab11a-positive vesicles accumulate at the midbody in a MICAL1-dependent manner. Disrupting the MyoVa/MICAL1 interaction leads to a largely decreased accumulation of both MyoVa and Rab11a-positive vesicles at the midbody and consequently prolongs the cytokinesis time. By solving the MyoVa/MICAL1 complex structure, we found that MICAL1 competes with Spires for the binding to MyoVa, which is further confirmed by our biochemical and cellular analysis. These results suggest that the regulatory balance between F-actin assembly and disassembly is important for the unloading of MyoVa-transported cargoes. The activity of MICAL1 for F-actin disassembly is required for the accumulations of MyoVa and Rab11a-positive vesicles at the midbody, further confirming the importance of actin dynamics in cargo unloading. Collectively, our results revealed that MyoVa, by a competitive recruitment of F-actin disassembly regulator MICAL1, controls its F-actin track disassembly to induce the unloading of Rab11a-positive vesicles.

[1]Department of Biology, Southern University of Science and Technology, Shenzhen, Guangdong, China. [2]Academy for Advanced Interdisciplinary Studies, Southern University of Science and Technology, Shenzhen, Guangdong, China. [3]Guangdong Provincial Key Laboratory of Cell Microenvironment and Disease Research, and Shenzhen Key Laboratory of Cell Microenvironment, Shenzhen, Guangdong, China. [4]Core Research Facilities, Southern University of Science and Technology, Shenzhen, Guangdong, China.
*These authors contributed equally to this work.
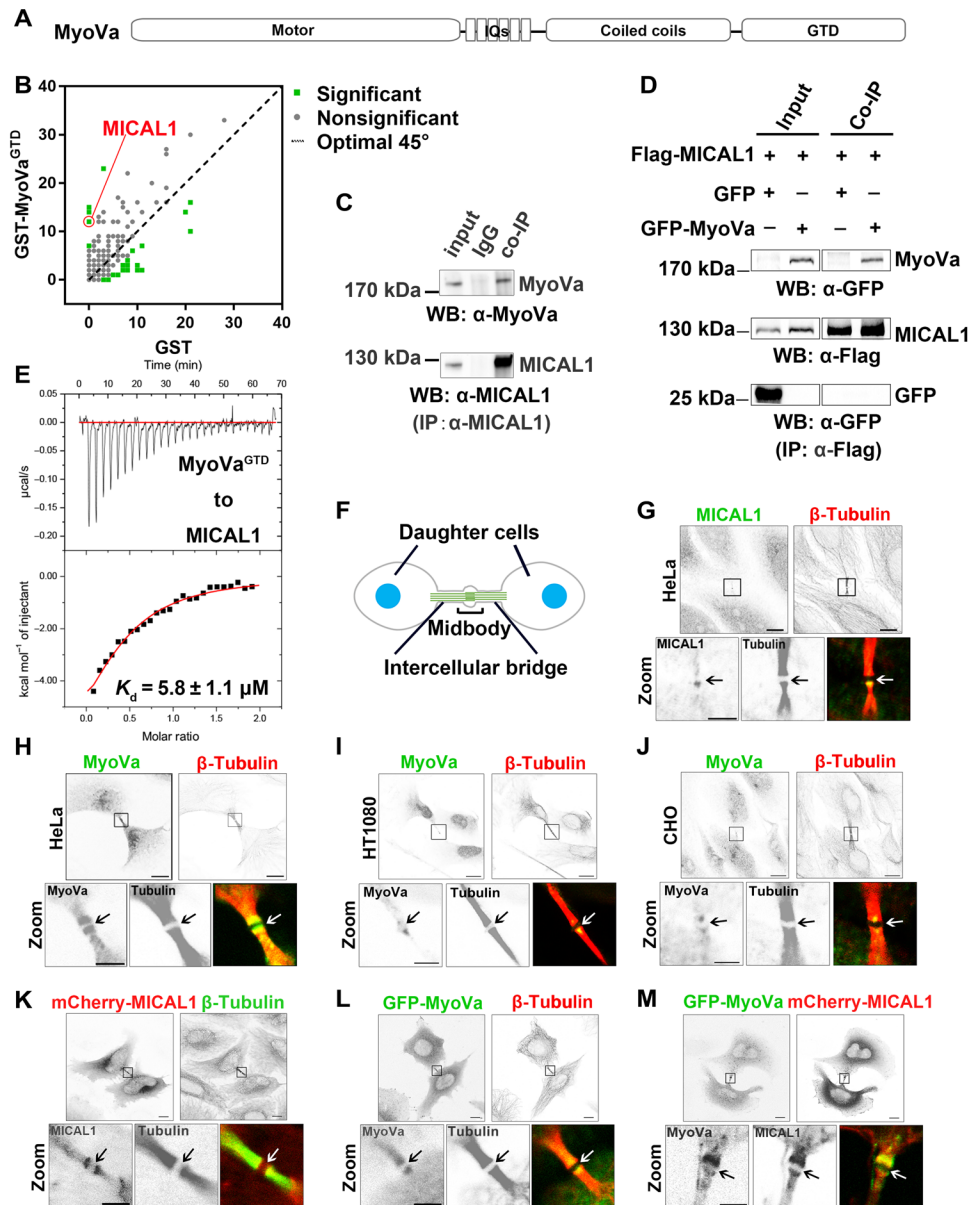†Corresponding author. Email: weizy@sustech.edu.cn (Z.W.); yuc@sustech.edu.cn (C.Y.)

Fig. 1. MyoVa and MICAL1 colocalized at the midbody via the direct interaction. (**A**) Domain architecture of MyoVa. (**B**) Quantitative scatterplot of the total spectra from the binding candidates of GST-MyoVa^{GTD} versus those of GST (control), based on the mass spectrum results of two GTS pull-down samples. $P < 0.05$, Fisher's exact test. (**C** to **E**) The interaction between endogenous (C) or overexpressed (D) MyoVa and MICAL1 was detected by co-IP and ITC (E) assays. (**F**) Schematic diagram represents midbody and intercellular bridge between two separating daughter cells during cytokinesis. Cell nucleus in two daughter cells and microtubules in intercellular bridge are indicated with blue circle and green line, respectively. (**G** to **J**) Accumulations of endogenous MICAL1 at the midbody in HeLa cells (G) and endogenous MyoVa at the midbodies in HeLa (H), HT1080 (I), and Chinese hamster ovary (CHO) cells (J) during cytokinesis by immunofluorescence. (**K** to **M**) HeLa cells were transfected with mCherry-MICAL1 (K) or green fluorescent protein (GFP)–MyoVa (L) individually and cotransfected with GFP-MyoVa and mCherry-MICAL1 (M). β-Tubulin was stained to indicate the intercellular bridge. In each panel, the regions containing midbodies were enlarged as Zoom views and the centers of the midbodies were indicated by arrows. Scale bars, 10 μm (upper views) and 3 μm (lower Zoom views). The image presentation model of the midbodies shown here was applied throughout the entire manuscript except as otherwise indicated.

RESULTS

MICAL1 is a previously unidentified binding partner of MyoVa at the midbody during cytokinesis

To uncover the regulation mechanism of MyoVa-mediated cargo transport, we aimed to identify new binding partners of the GTD (MyoVa^{GTD}), which is the major cargo binding region in MyoVa (Fig. 1A). By using glutathione S-transferase (GST) pull-down assay coupled with mass spectrum, we fished out some binding candidates of GST-MyoVa^{GTD} from mouse brain lysate (fig. S1A). As expected, several previously reported MyoVa^{GTD}-interacting proteins, such as Spir1 (28), Purα (35), and Rab3 (36), were detected (fig. S1B). A previously unknown candidate called MICAL1 (Fig. 1B and fig. S1B) that precisely controls F-actin dynamics (37, 38) aroused our attention, considering MyoVa as the actin-based motor.

First, we confirmed the physical interaction between MyoVa and MICAL1 by performing coimmunoprecipitation (co-IP) assay with both endogenous and transiently overexpressed proteins of MICAL1 and MyoVa in HeLa cells (Fig. 1, C and D) and GST pull-down assay using the purified proteins of the full-length MICAL1 and the MyoVa^{GTD} fragment (fig. S1C). The binding affinity between MICAL1 and MyoVa^{GTD} was measured with a K_d (dissociation constant) of ~6 μM by using isothermal titration calorimetry (ITC) (Fig. 1E). We then analyzed the subcellular localizations of endogenous MyoVa and MICAL1 in HeLa cells. Despite the robust in vitro interaction, the two individual proteins showed distinct distributions in the cytoplasm. MyoVa was distributed as puncta (fig. S1D), while MICAL1 was largely diffused (fig. S1E). However, by using β-tubulin as a marker of intercellular bridges for dividing cells during cytokinesis, we found that, in different types of cells, both MyoVa and MICAL1 highly accumulated on either one side or both sides of the midbody, a transient subcellular structure physically separating two daughter cells as a platform for the successful completion of abscission during cytokinesis (Fig. 1, F to J) (39, 40). In line with our biochemical findings, in cotransfected HeLa cells, MyoVa and MICAL1 colocalized well at both sides of the midbody during cytokinesis (Fig. 1, K to M).

Recruiting MyoVa to the midbody by MICAL1 is essential for cytokinesis

Given that MyoVa is one of the major motors for intracellular cargo transport, does MyoVa transport MICAL1 to the midbody? To address this question, we narrowed down a 23-residue fragment (residues 800 to 822) in MICAL1 (Fig. 2A), locating at the longest loop connecting the LIM and RBD (Rab-binding domain) domains, as the minimal MyoVa^{GTD}-binding motif (GTBM) by using analytical size exclusion chromatography (aSEC) and ITC-based measurement (fig. S2, A and B). The binding affinity (K_d of ~3 μM) of the GTBM fragment of MICAL1 (MICAL1^{GTBM}) to MyoVa^{GTD} is comparable to that of the full-length MICAL1, indicating that MICAL1^{GTBM} was sufficient for the binding of MICAL1 to MyoVa. Notably, sequence analysis identified the conserved GTBM sequence in the mammalian MICAL1 proteins but not in two other members MICAL2 or MICAL3 in MICAL family (fig. S2C), suggesting that MyoVa specifically interacts with MICAL1. Next, we removed the GTBM fragment from MICAL1 to create a MyoVa-binding deficient construct (MICAL1^{ΔGTBM}), which was validated using co-IP assay (fig. S2D). MICAL1^{ΔGTBM} retains its localization at the midbody (fig. S2E), implicating that the midbody localization of MICAL1 is independent of MyoVa. Instead, by using the small interfering RNA (siRNA)–mediated knockdown of MICAL1 (MICAL1^{KD}) in HeLa cells (fig. S3A), we found that endogenous MyoVa lost its localization at the midbody (Fig. 2, B, C, and F). The deficiency of the midbody localization was completely rescued by the overexpression of the wild-type MICAL1 protein (Fig. 2, D and F). In contrast, expressing the MICAL1^{ΔGTBM} mutant failed to restore the midbody localization of the endogenous MyoVa (Fig. 2, E and F), although the wild-type MICAL1 and MICAL1^{ΔGTBM} proteins showed similar protein levels at the midbody (Fig. 2G). Thus, the binding of MyoVa to MICAL1 is critical for the midbody localization of MyoVa.

As a protein-dense structure physically separating two daughter cells, the midbody is essential for completing the final stages of cytokinesis, especially the abscission process (39, 40). Because MICAL1 was reported to be an essential regulator in cytokinesis (41), the in-

teraction between MyoVa and MICAL1 at the midbody may contribute to the cytokinesis process. To test this possibility, we generated the MyoVa knockout (MyoVa^{KO}) and MICAL1 knockout (MICAL1^{KO}) HeLa cells by using CRISPR-Cas9 gene-editing technique (fig. S3, B to G). Consistent with the observation in the MICAL1^{KD} HeLa cells, the depletion of MICAL1 prevented endogenous MyoVa from locating at the midbody (fig. S3, H and I) and the overexpression of wild-type MICAL1, but not MICAL1^{ΔGTBM}, restored the midbody localization of MyoVa (fig. S3I). With the MICAL1^{KO} and MyoVa^{KO} cells, we performed live cell imaging and analyzed the impact of either MICAL1 or MyoVa on the process of cytokinesis (fig. S4, A and B). Consistent with the reported function of MICAL1 during cytokinesis (41), the abscission finished with a significant delay of ~73 min for the MICAL1^{KO} cells, comparing to that for normal HeLa cells (Fig. 2H). Similarly, the cytokinesis time was prolonged by ~50 min for MyoVa^{KO} cells (Fig. 2H), indicating that MyoVa also plays an important role in cytokinesis. To confirm that the function of MyoVa in cytokinesis is mediated by MICAL1, we transfected either mCherry-tagged wild-type MICAL1 or MyoVa-binding deficient mutant MICAL1^{ΔGTBM} into the MICAL1^{KO} cells (fig. S4C). As a result, the mCherry-MICAL1 overexpression fully restored the delayed cytokinesis in MICAL1^{KO} cells. In contrast, the MICAL1^{KO} cells expressing the similar level of mCherry-MICAL1^{ΔGTBM} showed a delayed cytokinesis time comparable with the MICAL1^{KO} cells expressing mCherry only (Fig. 2I and fig. S4D). Together, our biochemical and cellular analysis demonstrated that MyoVa plays an essential role in the process of cytokinesis by interacting with MICAL1 at the midbody.

MyoVa-mediated transport of Rab11a-positive vesicles to the midbody is regulated by MICAL1

How does MyoVa participate in cytokinesis by interacting with MICAL1? Because MICAL1 regulates the cytokinesis through the oxidation-mediated depolymerization of F-actin at the midbody (41), we speculated that the catalytic activity of MICAL1 on F-actin may be regulated by forming the complex with MyoVa. However, the NADPH [reduced form of nicotinamide adenine dinucleotide phosphate (NADP$^+$)] consumption analysis indicated that the presence of MyoVa^{GTD} has little impact on the activity of MICAL1 (fig. S5A). Considering that the membrane supplied by endosomal trafficking is required for the completion of cytokinesis (31, 42, 43) and MyoVa is a classical actin-based transporter for diverse intracellular vesicles (15, 36), we hypothesized that MICAL1 regulates the MyoVa-mediated vesicle transport to the midbody and thereby promotes the abscission event during cytokinesis. Because Rab11 is a well-known cargo adaptor of MyoVa for recycling endosome transport (Fig. 3, A and B) (28, 36) and Rab11-positive vesicles accumulate at the midbody to provide membrane and signaling components required for cytokinesis (32–34), it is likely that Rab11-positive vesicles are transported to the midbody by MyoVa. As expected, the overexpressed Rab11a formed puncta in the cytoplasm and were significantly concentrated at the midbody during cytokinesis (Fig. 3C). On the basis of the MyoVa/Rab11a complex structure determined previously (Fig. 3A) (28), we designed a mutant, Rab11a-F48Q, which impaired the MyoVa-binding capacity of Rab11a (Fig. 3B). Similar to the wild-type Rab11a protein, Rab11a-F48Q still formed puncta in the cytoplasmic region, suggesting that this mutant remains the association with vesicles (Fig. 3D). However, unlike the wild-type Rab11a, Rab11a-F48Q lost the enrichment at the midbody
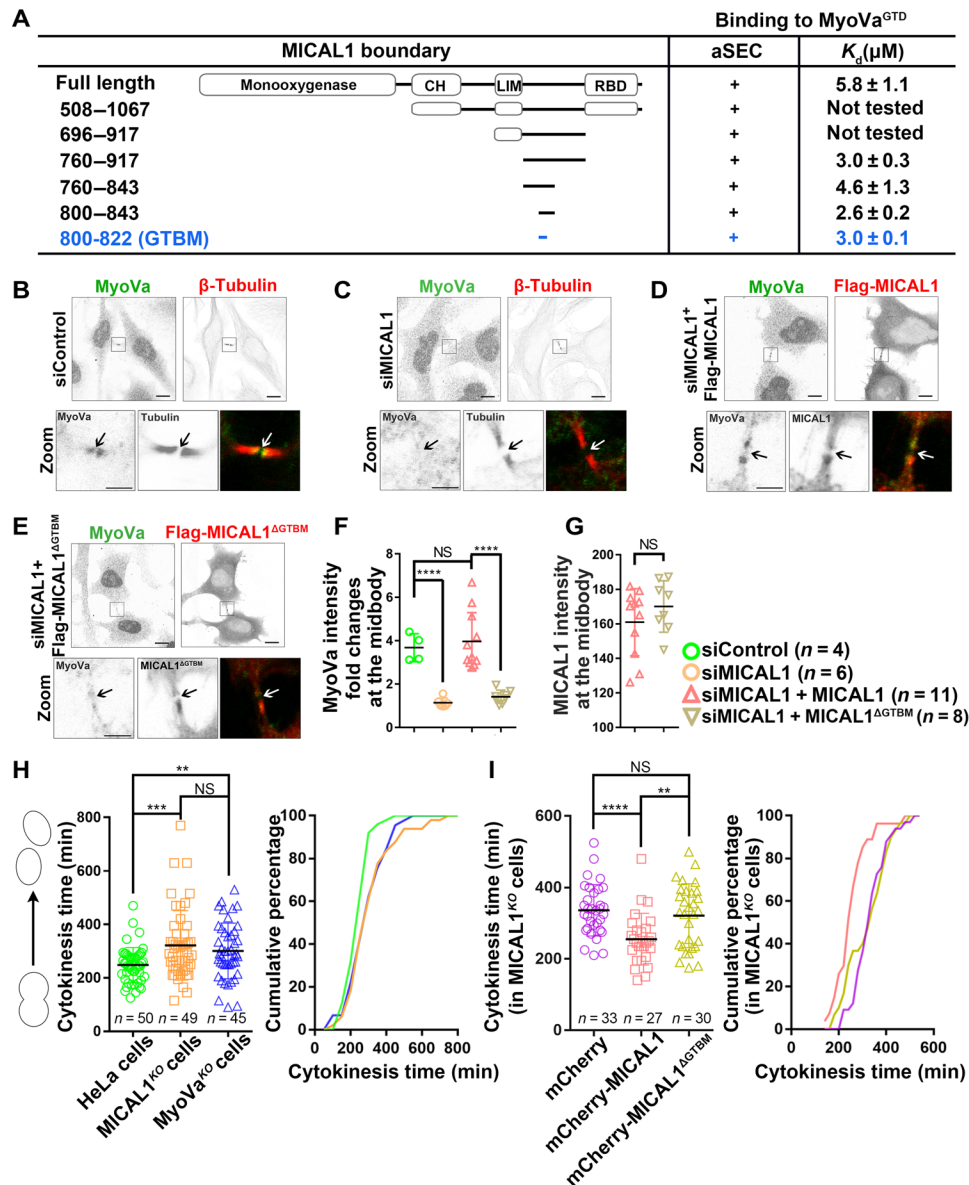
Fig. 2. The interaction between MICAL1 and MyoVa at the midbody is essential for efficient cytokinesis. (A) The GTD-binding motif (GTBM) in MICAL1 was mapped into a loop region connecting LIM and CC domains. Detailed data were shown in fig. S2. (B and C) HeLa cells were treated with the control siRNA (siControl) (B) or the siRNA targeting the MICAL1 mRNA (siMICAL1) (C) for 72 hours and then stained by the antibody against MyoVa. (D and E) In the MICAL1^{KD} cells, Flag-tagged MICAL1 (D) or MICAL1$^{\Delta GTBM}$ (E) was transfected for additional 24 hours to rescue the midbody accumulation of MyoVa. Endogenous MyoVa and overexpressed Flag-MICAL1/MICA1$^{\Delta GTBM}$ were stained with the antibodies against MyoVa and Flag, respectively. (F and G) Statistical analysis of the intensity fold change of accumulated MyoVa at the midbody (F) and the intensity of overexpressed Flag-MICAL1/MICAL1$^{\Delta GTBM}$ at the midbody (G) in siRNA-treated HeLa cells. The fold change represents the MyoVa intensity change ratio between the midbody and its adjacent region. The fold change value around 1 indicates diffused distribution at the midbody, while the value larger than 1 indicates accumulation happening at the midbody. Intensity was detected by ImageJ, and cell number for analysis per condition was indicated. (H) Statistical analysis of cytokinesis time, from furrow ingression to abscission completion as indicated on the left, in normal and knockout HeLa cells. (I) Rescue effects on the cytokinesis time of the MICAL1^{KO} cells transfected with empty mCherry vector, mCherry-MICAL1, and mCherry-MICAL1$^{\Delta GTBM}$. The corresponding cumulative percentage plot was present to show the distribution of cytokinesis time. The cytokinesis time of the indicated number of cells was measured per condition, and measurement details are shown in fig. S4.

(Fig. 3, D and F), supporting the idea that the recruitment of Rab11a to the midbody is mediated by MyoVa. Hence, MyoVa facilitates the cytokinesis process by transporting the Rab11a-positive vesicles to the midbody.

To further investigate whether MICAL1 is involved in the MyoVa-mediated vesicle transport to the midbody via the direct interaction between MyoVa and MICAL1, we detected the distribution of Rab11-positive vesicles in the MICAL1^{KO} cells by the transient transfection of Rab11a. In contrast to the enrichment of Rab11a at the midbody in the normal HeLa cells (Fig. 3C), Rab11a showed a largely diffused distribution in the intercellular bridge in the MICAL1^{KO} cells during cytokinesis (Fig. 3G). Consistently, the
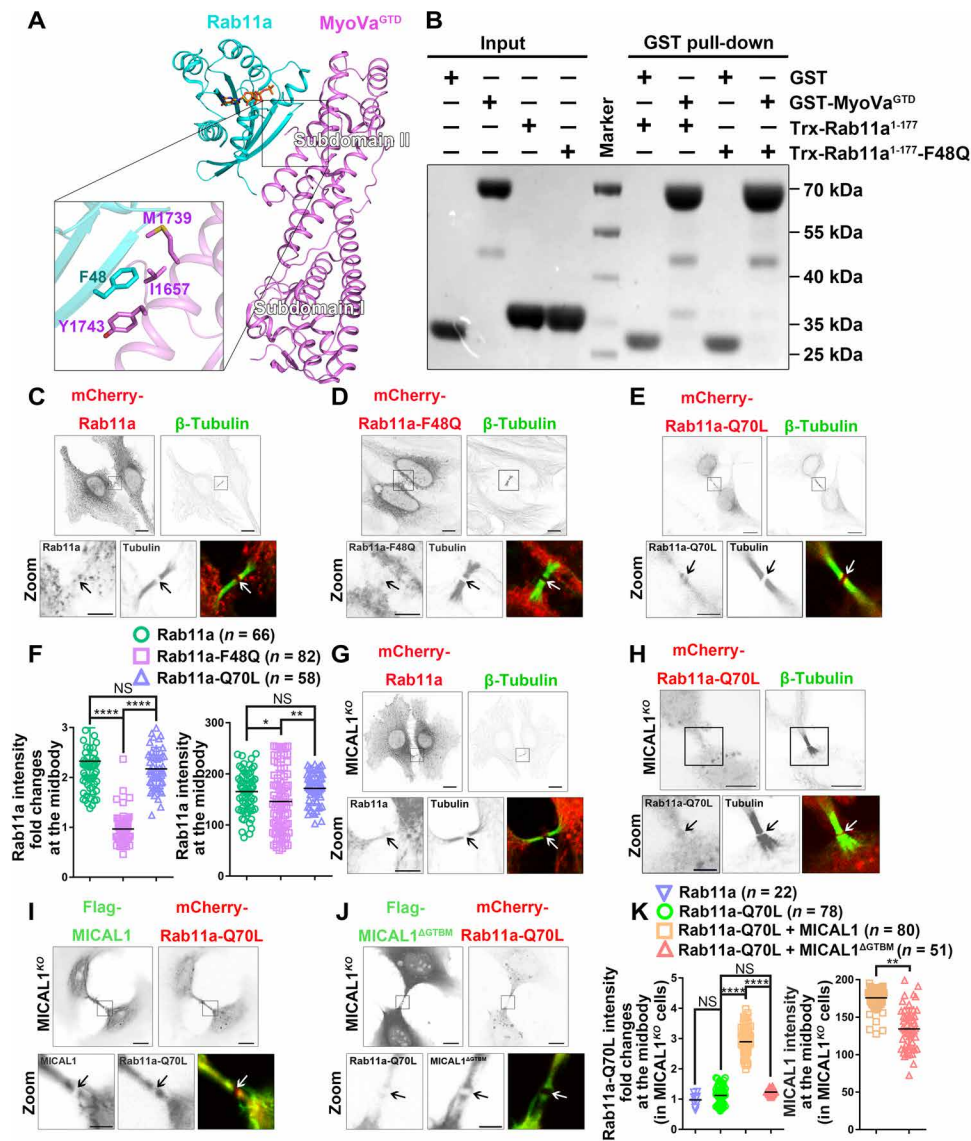
Fig. 3. MICAL1 coordinates Rab11a-positive vesicle trafficking to the midbody by interacting with MyoVa. (**A**) Complex structure of MyoVa^{GTD} (purple) and Rab11a (cyan) [Protein Data Bank (PDB) ID: 5JCZ] (*28*). Inset: Key residue F48 in Rab11a is inserted into the hydrophobic patch in subdomain II of MyoVa^{GTD}. (**B**) GST pull-down assay confirmed that Rab11a$^{1-177}$ directly bound to MyoVa^{GTD}, while the Rab11a$^{1-177}$-F48Q mutant abolished the binding. The gel was stained by Coomassie blue. (**C** to **E**) Midbody localization of Rab11a in the HeLa cells transfected with mCherry-tagged Rab11a (C) or Rab11a-F48Q (D) or Rab11a-Q70L (E). (**F**) Statistical analysis of the intensity fold change and the intensity of overexpressed Rab11a or Rab11a-F48Q or Rab11a-Q70L at the midbody. The fold change represents the Rab11a intensity ratio between the midbody and its adjacent region. Cell number per condition for analysis was indicated. (**G** and **H**) Midbody localization of Rab11a in the MICAL1^{KO} cells transfected with the mCherry-tagged Rab11a (G) or Rab11a-Q70L (H), the constitutively active mutant of Rab11a. (**I** and **J**) Rescue assay was performed by overexpression of Flag-tagged MICAL1 (I) or MICAL1$^{\Delta GTBM}$ (J) in MICAL1^{KO} cells cotransfected with mCherry-tagged Rab11a-Q70L. (**K**) Statistical analysis of the intensity fold change of mCherry-tagged Rab11a-Q70L and the intensity of overexpressed Flag-MICAL1/MICAL1$^{\Delta GTBM}$ at the midbody in MICAL1^{KO} cells. The fold change represents the intensity change ratio of Rab11a-Q70L between the midbody and its adjacent region. Cell number per condition for analysis was indicated.

constitutively active mutant Rab11a-Q70L, which is a predominant guanosine triphosphate (GTP)–bound state to effectively and stably link MyoVa with transporting vesicles (*36*, *44*), enriched at the two sides of the midbody in the normal HeLa cells (Fig. 3, E and F), but not in the MICAL1^{KO} cells (Fig. 3, H and K). Because MICAL1 does not directly interact with Rab11a (*45*), it is likely that MICAL1 drives the accumulation of Rab11a-positive vesicles at the midbody by binding to MyoVa. Compared with the partially recovered enrichment

of Rab11a-Q70L at the midbody in the MICAL1^{KO} cells expressing Flag-tagged MICAL1 (Fig. 3, I and K), the accumulation of Rab11a-Q70L at the midbody completely failed to be recovered in the MICAL1^{KO} cells expressing Flag-MICAL1$^{\Delta GTBM}$ (Fig. 3, J and K), confirming the critical role of the MyoVa/MICAL1 interaction for the distribution of the Rab11a-positive vesicles at the midbody. Together, our data demonstrate that MICAL1 regulates the MyoVa-mediated vesicle transport to accumulate at the midbody for efficient cytokinesis.

Because the depletion of MICAL1 results in the F-actin enrichment at the intercellular bridge (fig. S5, B and C) (41), it is also possible that the high F-actin level prevents Rab11a-positive vesicles from accumulating at the midbody. To rule out this possibility, we overexpressed wild-type MICAL1, MICAL1$^{\Delta GTBM}$, and the catalytically inactive mutant MICAL1-3G3W (41) in the MICAL1^{KO} cells and analyzed the F-actin level at the intercellular bridge. As expected, the overexpression of MICAL1, but not the catalytically inactive mutant, significantly decreased the F-actin level at the midbody (fig. S5D). Overexpressing MICAL1$^{\Delta GTBM}$ also reduced the midbody F-actins to the level similar to those in the cells overexpressing MICAL1 (fig. S5D). As the midbody localization of Rab11 was disrupted by the ΔGTBM mutant, the F-actin analysis here provided additional evidence to support that the accumulation of Rab11a-positive vesicles at the midbody depends on the MyoVa/MICAL1 interaction rather than the F-actin level.

MICAL1 determines the unloading of the MyoVa-transported Rab11a-positive vesicles at the midbody

The impaired accumulation of the Rab11a-positive vesicles at the midbody in the MICAL1^{KO} cells suggests that the loss of MICAL1 results in the dysfunction of the MyoVa-mediated vesicle transport. To uncover the roles of MICAL1 acting in the MyoVa-mediated vesicle transport at the midbody, we monitored the movements of the Rab11a-positive vesicles in real time by transiently transfecting cells with mCherry-Rab11a-Q70L as the marker of MyoVa-transporting vesicles (fig. S5, E and F). In normal HeLa cells, the Rab11a-positive vesicles move from the cell bodies to the midbody. A portion of the vesicles was observed to quickly contact each other and fuse into the highly concentrated Rab11a density at either one side or both sides of the midbody (Fig. 4A and movie S1), where MICAL1 is highly accumulated (Fig. 1G). In the MICAL1^{KO} cells, although the Rab11a-positive vesicles successfully reached the side of the midbody, the arrived vesicle was unable to be successfully docked for accumulation (Fig. 4B and movie S2). Thus, rather than attracting the MyoVa-transported vesicles to the midbody, MICAL1 docks the MyoVa and therefore promotes the accumulation of the vesicles transported by MyoVa at the midbody.

To further clarify the role of MICAL1 on the MyoVa-mediated vesicle transport at the midbody, we also analyzed the dynamics of the newly arrived MyoVa-transporting Rab11a-positive vesicles at the midbody by using the fluorescence recovery after photobleaching (FRAP) method. In the normal HeLa cells, after bleaching, the fluorescence signals of green fluorescent protein (GFP)–MyoVa and mCherry-Rab11a-Q70L at the midbody were quickly recovered to approximately 70 and 60% of the original level in 150 s, respectively (Fig. 4, C and E, and movie S3). In contrast, in the MICAL1^{KO} cells, less than 10% of the recovery for both GFP-MyoVa and mCherry-Rab11a-Q70L happened in the corresponding time (Fig. 4, D and E, and movie S4), indicating that the depletion of MICAL1 relieves the restriction on the MyoVa-mediated transport of Rab11a-positive vesicles at the midbody.

To determine whether MyoVa moves away from the midbody, we used the photoactivation assay by transfecting photoactivatable GFP (PAGFP)–tagged Rab11a-Q70L or MyoVa plasmids to the normal and MICAL1^{KO} cells. After photoactivation at the midbody, we measured the real-time intensity change of PAGFP signals at the midbody or the cytosol region (Fig. 4F). As a result, the intensity of Rab11a-Q70L at the midbody was decreased less than that at the cytosol region in the normal cells (Fig. 4G), confirming that Rab11-positive vesicles have a lower mobility at the midbody. Despite the fact that the intensity changes of Rab11a-Q70L and MyoVa at the cytosol in the normal and MICAL1^{KO} cells are essentially identical (Fig. 4H), the Rab11a-Q70L and MyoVa intensities at the midbody in the MICAL1^{KO} cells were decreased much faster than did those observed in the normal cells (Fig. 4I), supporting the idea that MICAL1 prevents Rab11-positive vesicles from leaving the midbody by associating with MyoVa. Consistent with the FRAP results indicating that MyoVa is more dynamic than Rab11a-Q70L at the midbody (Fig. 4E), the MyoVa intensity in the photoactivation assay showed a faster decreasing curve compared with that of Rab11a-Q70L at the midbody in the normal cells (Fig. 4I). This observation further suggests that MyoVa tends to leave the midbody after the cargo unloading. In addition, we measured the flux of PAGFP-Rab11a-Q70L signals at the intercellular bridge after photoactivating a neighboring cytosol region (fig. S5G). The PAGFP intensity increases observed in the normal and MICAL1^{KO} cells were similar, further indicating that the depletion of MICAL1 does not prevent Rab11-positive vesicles from entering the intercellular bridge but inhibits the release of Rab11-positive vesicles at the midbody, the transporting destination. Together, we confirmed that, based on the direct interaction with MyoVa, MICAL1 docks MyoVa to induce the unloading of the MyoVa-transported Rab11a-positive vesicles at the midbody (Fig. 4J).

Overall structure of the MyoVa^{GTD}/MICAL1^{GTBM} complex

The above cellular analysis of the Rab11a-positive vesicles raises the question of how MICAL1, by interacting with MyoVa, regulates the unloading of the transported vesicle at the midbody. To gain insights into the molecular basis underlying the MyoVa/MICAL1 interaction, we determined the crystal structure of the MyoVa^{GTD}/MICAL1^{GTBM} complex with a resolution of 1.6 Å (Fig. 5A and table S1). In one asymmetric unit, two essentially identical MyoVa^{GTD}/MICAL1^{GTBM} complexes were observed with a GTD-GTBM binding ratio of 1:1. MyoVa^{GTD} shows a highly similar conformation with the previously solved GTD structures (fig. S6A) (46), containing two helical subdomains, subdomains I and II (Fig. 5A). The MICAL1^{GTBM} peptide, clearly assigned with an N-terminal loop and a C-terminal α helix (Fig. 5A and fig. S6B), interacts with helices α4, α5, and α8 in subdomain I of MyoVa^{GTD} (Fig. 5A). The binding of MICAL1^{GTBM} to MyoVa^{GTD} is largely mediated by hydrophobic interactions. The four strictly conserved hydrophobic residues I806, L808, L816, and L819 in MICAL1^{GTBM} pack with a hydrophobic groove formed by hydrophobic residues of α4 and α8 in MyoVa^{GTD} (fig. S6, C to E). Consistently, mutating these hydrophobic residues in MICAL1^{GTBM} or in MyoVa^{GTD} (e.g., I1559) to hydrophilic residues abolished the MyoVa/MICAL1 interaction in solution (fig. S6, G and H). In addition to the hydrophobic interactions, several positively charged residues contribute to the MyoVa^{GTD}/MICAL1^{GTBM} interaction. R803 and R804 in MICAL1^{GTBM} insert their side chains into a negatively charged surface patch formed by two loops connecting helices α5 and α6 and helices α7 and α8 of MyoVa^{GTD}, respectively, while R804 in MICAL1^{GTBM} forms salt bridges with D1548 in MyoVa^{GTD} (fig. S6, D and F). The ITC-based analysis also confirmed that disruption of these charge-charge interactions diminishes the interaction (fig. S6, G and H). In addition, the N terminus and C terminus of MICAL1^{GTBM} face to the negatively and positively charged
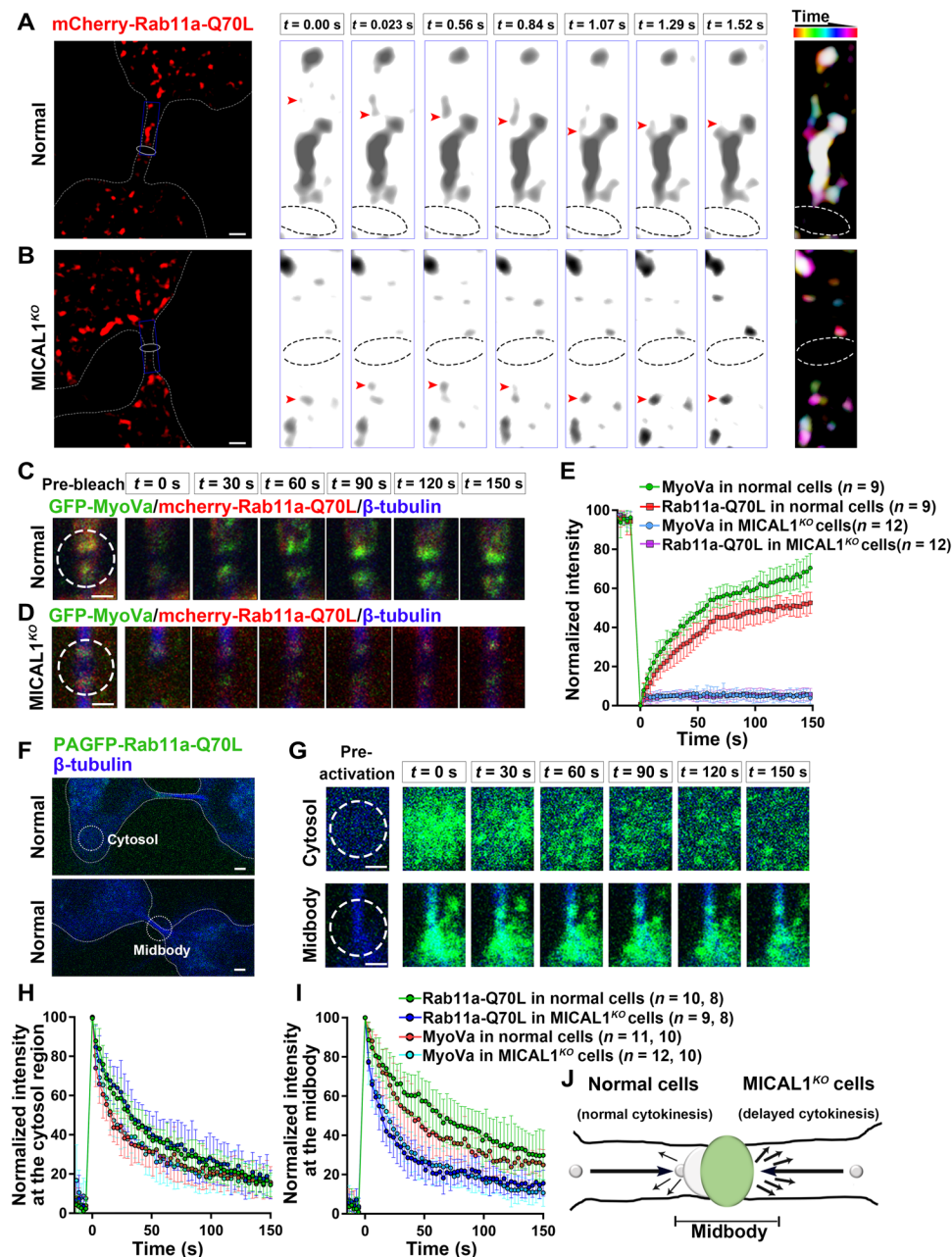
Fig. 4. MICAL1 controls the unloading of Rab11a-positive vesicles at the midbody. (**A** and **B**) Normal (A) and MICAL1^{KO} cells (B) expressing mCherry-Rab11a-Q70L were observed under a time-scaled SIM. The boundaries of two daughter cells during cytokinesis were indicated with dashed lines, and the middle regions of midbody were circled. Scale bars, 1 μm. The midbody regions were enlarged in the time-series snapshots to show the movements of Rab11a-positive vesicles indicated by red arrowheads. The corresponding overlapped figures in the right panel were calculated under time-lapse color mode by ImageJ. (**C** and **D**) FRAP analysis of Rab11a-positive vesicles at the midbody in normal (C) and MICAL1^{KO} cells (D) expressing GFP-MyoVa and mCherry-Rab11a-Q70L. The bleaching region was indicated by a dashed circle, and β-tubulin was stained with SiR-tubulin to indicate the intercellular bridges. Scale bars, 1 μm. (**E**) Recovery efficiency of GFP-MyoVa and mCherry-Rab11a-Q70L at the midbody. Cell number per condition for analysis was indicated. (**F**) HeLa cells expressing PAGFP-tagged Rab11a-Q70L were photoactivated at the midbody region or the cytosol region. The two regions were indicated by dashed circles. Scale bars, 1 μm. (**G**) The intensity changes of the two regions shown in (F) were recorded and shown in a time-series snapshots. Scale bars, 1 μm. (**H** and **I**) Normalized intensity analysis of photoactivated PAGFP-tagged Rab11a-Q70L and MyoVa at the cytosol (H) and midbody (I) in the normal or MICAL1^{KO} cells. Cell number per condition was indicated for the analysis in the cytosol and midbody regions. (**J**) Schematic cartoon to illustrate the observed motion of the Rab11a-positive vesicles (gray balls) at the midbody controlled by MICAL1.

surface on MyoVa^{GTD}, respectively (fig. S6F). Such an asymmetric surface charge distribution of MyoVa^{GTD} facilitates the MICAL1^{GTBM} peptide to adopt the correct orientation upon binding. Because the interface residues of MyoVa^{GTD} are highly con-

served (46), the MICAL1-binding mode is very likely to be shared by all class V myosins in mammals. Consistently, MyoVb^{GTD} bound to MICAL1^{GTBM} with a comparable binding affinity (K_d of ~6 μM) (fig. S6I).
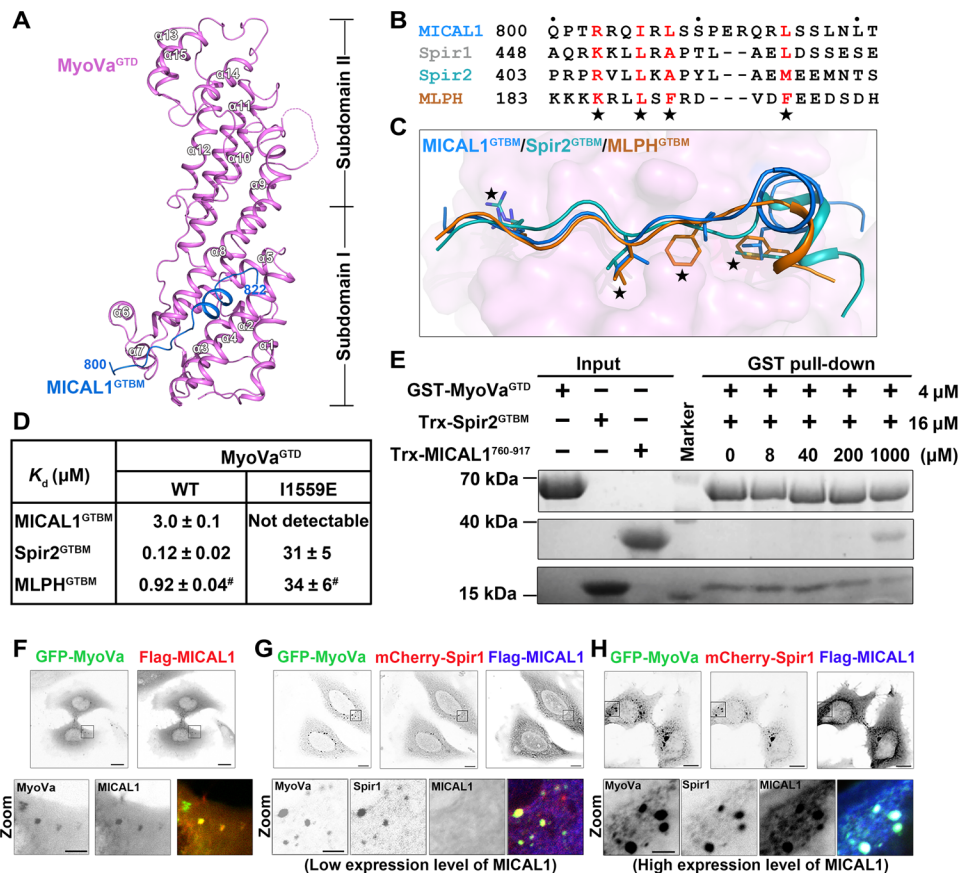
Fig. 5. MICAL1 competes with Spires in binding with MyoVa. (**A**) Cartoon representation of the overall structure of MyoVa^{GTD} (purple) in complex with MICAL1^{GTBM} (blue). The GTBM region of MICAL1 binds to the subdomain I of MyoVa^{GTD}. (**B**) Structure-based sequence alignment of the GTBM regions from MICAL1, Spir1/2, and MLPH. The residues important for the interaction with MyoVa^{GTD} were highlighted in red and indicated by stars. (**C**) Structural comparison of the MyoVa^{GTD}-bound GTBMs in MICAL1 (blue), Spir2 (cyan, PDB ID: 5JCY), and MLPH (orange, PDB ID: 4KP3). The surface of MyoVa^{GTD} was shown in light purple. The main interface residues of the three GTBM peptides were shown as sticks, corresponding to the highlighted residues in (B). (**D**) ITC-derived binding affinity between MyoVa^{GTD} or MyoVa^{GTD}-I1559E and the three GTBM peptides. #, previously reported binding affinity (46). (**E**) GST pull-down assay was performed to confirm the competition between Spir2 and MICAL1 in the binding to MyoVa. The gel was stained by Coomassie blue. (**F**) Confocal imaging of HeLa cells cotransfected with GFP-MyoVa and Flag-MICAL1. (**G** and **H**) Confocal imaging of HeLa cells triple-transfected with GFP-MyoVa, Flag-MICAL1, and mCherry-Spir1. Cells with relatively low (G) and high (H) expression of Flag-MICAL1 were compared.

MICAL1 competes with Spires on the binding to MyoVa in a concentration-dependent manner

The MICAL1-binding surface on MyoVa^{GTD} is overlapped with the binding surfaces for melanophilin (MLPH) (46) and Spires (28) (Fig. 5, B and C), which are cargo adaptors of MyoVa. Despite the fact that the amino acid sequences of the GTBM motifs from MICAL1, Spire 1 (Spir1), Spire 2 (Spir2), and MLPH share little similarity, they interact with MyoVa^{GTD} with a similar binding mode, as indicated by their superimposed interface residues (Fig. 5, B and C, and fig. S7A). Supporting this finding, the MICAL1-binding deficient mutation, I1559E, in MyoVa^{GTD} also disrupts the bindings of MyoVa to both Spir2 and MLPH (Fig. 5D) (46). The major difference among the three binding modes is the different orientations of the C-terminal helical regions in the three GTBM motifs, contributing to the different binding affinities on MyoVa^{GTD} (Fig. 5D and fig. S7B). For example, Q1630 in MyoVa^{GTD} forms hydrogen bonds with the backbone of MICAL1^{GTBM}, while it participates in the interaction with neither Spir2^{GTBM} nor MLPH^{GTBM} (fig. S7B). Consistently, the Q1630V mutation weakened the binding of MyoVa^{GTD} to

MICAL1^{GTBM} but slightly affected the MyoVa^{GTD}/Spir2^{GTBM} interaction (fig. S7, C and D).

Our structural findings of the overlapped MICAL1/Spir2-binding surface on MyoVa immediately raise the possibility of the potential competition between MICAL1 and Spir2 for their bindings to MyoVa. Spir2 and its homolog Spir1 are actin nucleation factors and promote F-actin assembly (17, 47), functionally antagonizing MICAL1 on actin dynamics. Because the Spire proteins are also essential for the MyoVa-mediated transport of Rab11-positive vesicles (27, 28), such a competition between the bindings of MICAL1 and Spires to MyoVa is likely to play a role in the MyoVa-mediated cargo transport. To confirm our structural observations, we performed an in vitro competition assay by using GST-MyoVa^{GTD} to pull down Spir2^{GTBM} in the presence of a GTBM-contained MICAL1 fragment (residues 760 to 917) with increasing concentrations. This MICAL1 fragment with a concentration of 1 mM, ~60-fold of the Spir2^{GTBM} concentration (16 µM), markedly decreased the MyoVa^{GTD}-bound fraction of Spir2^{GTBM} (Fig. 5E and fig. S8A). Meanwhile, the lower concentration of the MICAL1

fragment did not show an obvious competition on Spir2[GTBM] (Fig. 5E and fig. S8A). Such a concentration-dependent competition is in line with the observation that Spir2[GTBM] has a 25-fold higher MyoVa-binding affinity than MICAL1[GTBM] (Fig. 5D).

In cotransfected HeLa cells, overexpressed MyoVa and MICAL1 were colocalized as granule-like structures in the cytoplasm (Fig. 5F). Spires with much stronger MyoVa-binding affinity replaced MICAL1 at the MyoVa-positive granules when coexpressing MyoVa and MICAL1 with either Spir1 or Spir2 (Fig. 5G and fig. S8B). Consistent with the above structural and biochemical findings, in the triple-transfected HeLa cells with a high expression level of MICAL1, MICAL1 was found to accumulate at the MyoVa-positive granules containing Spir1 (Fig. 5H). Quantitative analysis of 17 triple-transfected cells with different expression levels of MICAL1 and Spir1 showed that the protein level of MICAL1 at the MyoVa-positive granules was increased with the increased overall MICAL1/Spir1 protein ratios (fig. S8C, left). In contrast, the protein level of Spir1 at the MyoVa-positive granules was negatively correlated with the overall MICAL1/Spir1 protein ratios (fig. S8C, right), confirming the concentration-dependent competition between MICAL1 and Spires on binding to MyoVa in cells. Considering that MICAL1 highly enriches at the midbody, while the Spir1 level decreases at the midbody compared to that at the intercellular bridge (fig. S8D), MICAL1 is able to outcompete Spires to bind with MyoVa at the midbody during cytokinesis.

MyoVa-transported cargo unloading depends on the catalytic activity of MICAL1 on F-actin disassembly

Because Spires and MICAL1 play opposite functions in tuning the assembly and disassembly of F-actin, the tracks for the MyoVa-mediated cargo transport, the concentration-dependent competitive binding of MICAL1 and Spires to MyoVa may provide a mechanistic explanation of how MICAL1 controls the unloading of the Rab11-positive vesicles at the midbody. As shown in fig. S8E, MyoVa recruits Spires to promote actin polymerization for the generation of F-actin for initializing transportation (28). Alternatively, MyoVa binds to MICAL1, the oxidase of actins for F-actin depolymerization (37, 38, 48), to collapse the F-actin and thereby cause transport termination to unload the cargoes at the midbody. To test whether the F-actin depolymerization activity of MICAL1 is required for the accumulation of MyoVa- and Rab11a-positive vesicles at the midbody, we generated the catalytically inactive mutant of MICAL1 (MICAL1-3G3W) by mutating three glycines to tryptophans in the consensus GXGXXG motif of the monooxygenase domain (49), which are critical for its cofactor FAD (flavin adenine dinucleotide) binding and for promoting F-actin disassembly (41, 48, 49). While still having the GTBM sequence for binding to MyoVa, MICAL1-3G3W lost its capability of recruiting both MyoVa- and Rab11a-positive vesicles to the midbody in the MICAL1[KO] cells (Fig. 6, A to D). Furthermore, our FRAP analysis showed that overexpressing the wild-type MICAL1 protein in the MICAL1[KO] cells resulted in ~35% recovery of Rab11a-positive vesicles at the midbody (Fig. 6, E and F, and movie S5), while overexpressing MICAL1-3G3W or MICAL1[ΔGTBM] diminished the recovery at the midbody (Fig. 6, E and F, and movies S6 and S7).

To determine whether the F-actin level at the midbody is important for the vesicle delivery, we treated the MICAL1[KO] cells overexpressing both mCherry-Rab11a-Q70L and GFP-MICAL1-3G3W with the nontoxic, low-dose (20 nM) F-actin depolymerizing drug latrunculin A (LatA) for 2 hours. The accumulation of Rab11-positive vesicles at the midbody was partially recovered (fig. S9, A to C), further confirming that MICAL1 regulates the unloading of Rab11-positive vesicles at the midbody via F-actin depolymerization. In addition, the LatA-treated MICAL1[KO] cells without the MICAL1-3G3W expression failed to rescue the Rab11a-Q70L accumulation at the midbody (fig. S9A), supporting the idea that the accumulation of Rab11-positive vesicles at the midbody requires not only the normal F-actin level but also the interaction between MyoVa and MICAL1. Therefore, the catalytic activity of MICAL1 that disassembles F-actin is required for the accumulations of MyoVa and its cargoes at the midbody, further indicating that MICAL1 mediates the unloading of MyoVa-transporting cargoes by associating with MyoVa as well as promoting F-actin disassembly.

DISCUSSION

Intracellular cargo transport is vital for various cellular processes. Cytokinesis, the final step of cell division, requires that numerous cellular membrane components are efficiently transported and precisely positioned to the midbody (31, 42, 43). Although the mechanisms of intracellular cargo transport mediated by cytoskeletal motors have been studied for decades, it is still largely a mystery how cargoes are unloaded when the transporters arrive at the destinations. In this study, we revealed that a classic actin-based motor, MyoVa, recruits MICAL1 to disassemble F-actin and therefore unloads Rab11-positive vesicles at the midbody to facilitate cytokinesis.

On the basis of our previous findings, we proposed a model for the regulation mechanism of the MyoVa-mediated cargo transport by recruiting different actin regulators, like MICAL1 and Spires (Fig. 6G). In this model, the resting MyoVa at the autoinhibited state (50, 51) is activated by binding to its cargoes or cargo adaptors (52–54), including Spires (28). By facilitating actin polymerization (28, 55) to supply walking tracks for MyoVa, Spires promote cargo transport at the initial stage. Given a much higher MyoVa-binding affinity of Spires over MICAL1 (Fig. 5D) and the similar overall protein levels of Spires and MICAL1 in cells (56, 57), it is unlikely that MICAL1 affects Spire-promoted cargo transport at most cytoplasmic regions. Once the transporting machine arrives at the destinations, such as the midbody, the highly enriched MICAL1 is able to compete out Spires from MyoVa (Fig. 5, E and H, and fig. S8D). Replacing Spires from MyoVa by activated MICAL1 not only inhibits the F-actin formation (49) but also promotes the F-actin disassembly (38, 58), thereby stopping MyoVa's walking and inducing cargo unloading. Last, as the relatively weak association between MyoVa and MICAL1 facilitates the dissociation of MICAL1 from MyoVa, MyoVa folds back more easily to the autoinhibited state, recycled for the next transport (Fig. 6G). Like MyoVa, MyoVb shows the similar binding capability with MICAL1 (fig. S6I) and Spires (28), suggesting that MyoVb shares the similar cargo unloading mechanism with MyoVa. Considering the complexity of the midbody (40), other unknown factors may be involved in the unloading process at the midbody (Fig. 6G). Nevertheless, the competition between Spires and MICAL1 provides a feasible mechanism for the unloading of MyoV transported cargoes, which still need further investigations. In addition, because MICAL1 regulates the cortical actin filament in the midbody region (41), the normal organization of the actin cortex may also participate in the MyoVa-mediated vesicle transport for efficient cytokinesis.
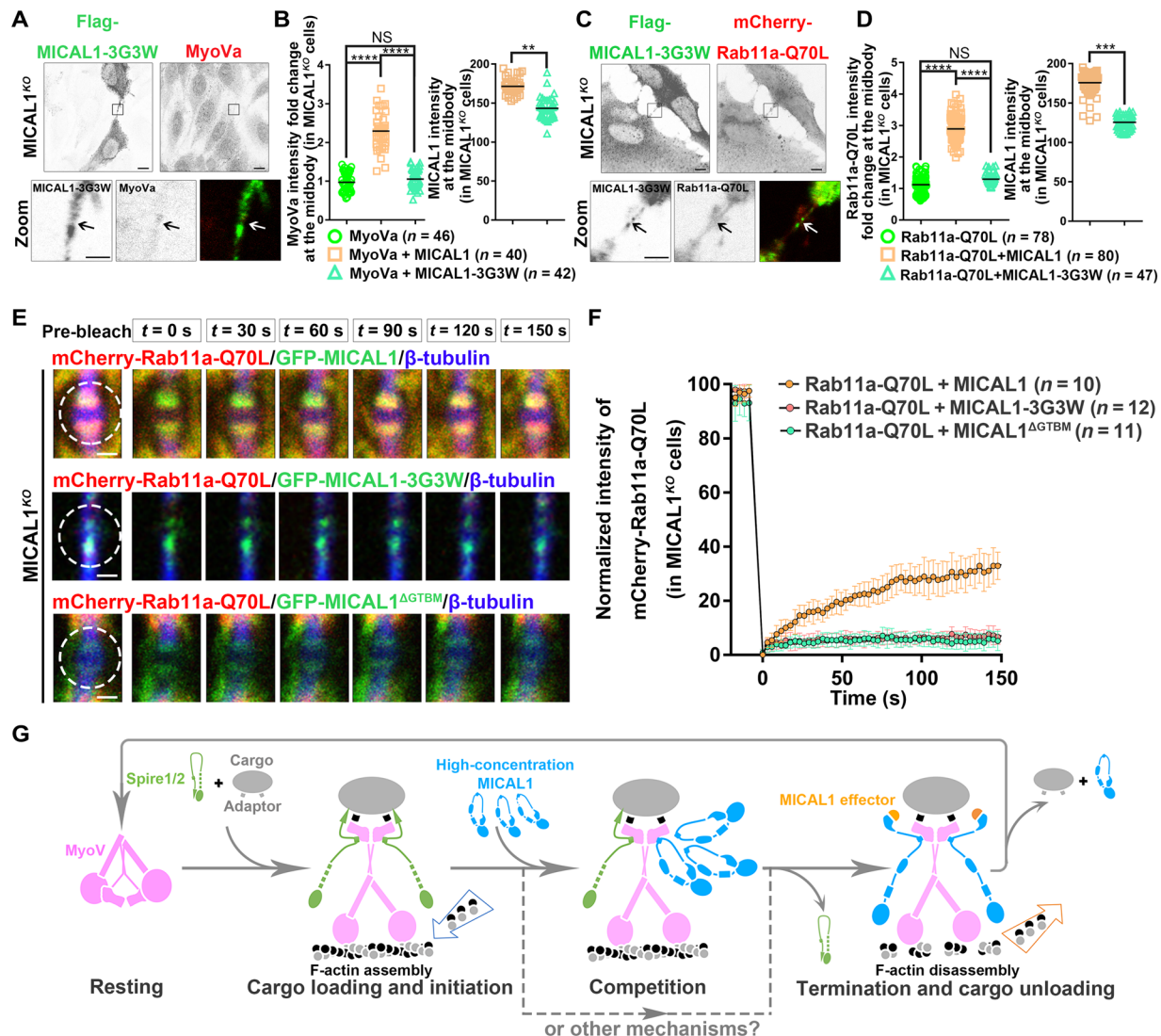
Fig. 6. Enzymatic activity of MICAL1 is required for Rab11a-positive vesicle unloading at the midbody. (**A** to **D**) Overexpression of the catalytically inactive MICAL1-3G3W mutant in MICAL1^{KO} cells failed to rescue the midbody accumulation of either endogenous MyoVa (A) or overexpressed Rab11a-Q70L (C). Statistical analysis of the intensity fold change of endogenous MyoVa (B) and Rab11a-Q70L (D) and the corresponding intensity of overexpressed MICAL1 at the midbody in MICAL1^{KO} cells, respectively. The fold change represents the MyoVa or Rab11a intensity ratio between the midbody and its adjacent region. Cell number per condition for analysis was indicated. (**E**) FRAP analysis of Rab11a-positive vesicles at the midbody in the MICAL1^{KO} cells coexpressing mCherry-Rab11a-Q70L with GFP-tagged MICAL1, MICAL1-3G3W, or MICAL1$^{\Delta GTBM}$. The bleaching region was indicated by a dashed circle, and β-tubulin was stained with SiR-tubulin to indicate the intercellular bridge. Scale bars, 1 μm. (**F**) Recovery efficiency of Rab11a-postive vesicles at the midbody in the MICAL1^{KO} cells cotransfected with mCherry-Rab11a-Q70L and GFP-tagged MICAL1, MICAL1-3G3W, or GFP-MICAL1$^{\Delta GTBM}$. Cell number per condition for analysis was indicated. (**G**) Proposed model for regulation mechanism of MyoV-mediated cargo transport by two mutually antagonistic F-actin regulators.

Because MyoVa transports diverse cargoes to different cellular locations, the cargo unloading mechanism that we found at the midbody likely exists at other places. For example, MICAL1 was found to regulate the distribution of Rab6-positive secretory vesicles, also the cargoes of MyoVa (*36*), at the growth cone in neurons (*59*). This is consistent with the idea that MICAL1 can be recruited and activated by a range of MICAL1 effectors, including small guanosine triphosphatases (GTPases) (*45*), which enrich at the different subcellular locations spatially and temporally. We noted with interests that other MICAL family members also play essential roles in intracellular trafficking, such as MICAL3 for Rab8a-positive ves-

icles transport (*60*). Whether these MICAL family proteins mediate cargo unloading for myosins needs further investigations.

The balance of F-actin assembly and disassembly regulated by Spires and MICAL1 is critical for the cargo transport mediated by an actin-based MyoVa motor. A similar regulation balance mediated by TTLL-11 glutamylase and CCPP-1 deglutamylase, two functionally opposite microtubule regulators in *Caenorhabditis elegans*, was reported to regulate the moving velocity of microtubule-based kinesin-2 and kinesin-3 motors (*61*). Likewise, several myosins have been found to interact with different F-actin regulators during cargo transport (*62–65*). Hence, we speculated that many cytoskeletal

motors adopt a similar mechanism to control the cargo transport by balancing the assembly and disassembly of cytoskeletal tracks.

Previously, very limited mechanisms for cargo unloading in motor-mediated transports have been suggested, including the exchange of small GTPase activity, phosphorylation, and adaptor degradation (11, 54, 66–70). However, these mechanisms largely rely on the changes of the protein properties. In contrast, by modifying F-actin to control the termination of molecular motors and induce positioning of the transported cargoes at their destinations, the cargo-unloading mechanism found in our study depends merely on differing protein concentrations of cytoskeletal regulators at different cellular locations and different cell states, providing a simple yet elegant method for efficient cargo delivery in cells.

MATERIALS AND METHODS
Affinity purification from mouse brain lysate coupled with mass spectrum analysis
To prepare mouse brain lysate, brains were extracted from about 2-month-old mouse and lysed in the buffer containing 20 mM CHAPS, 600 mM NaCl, 0.1% Triton X-100, protease inhibitors (cocktail), 1 mM EDTA, 1 mM EGTA, and 1 mM dithiothreitol (DTT) by using a tissue-type Dounce homogenizer. After ultracentrifuge, supernatants were dialyzed into the dialysis buffer of 20 mM Hepes, 100 mM NaCl, 5% glycerol, 1 mM EDTA, 1 mM EGTA, and 1 mM DTT. The brain lysate was obtained by using additional ultracentrifuge to remove the precipitants, and the total protein concentration was measured by Bradford assay. All the above procedures were performed at 4°C.

Purified GST or GST-MyoVa^{GTD} was first incubated with 40 μl of glutathione Sepharose 4 beads at 4°C for 30 min, followed by washes three times in the dialysis buffer with a supplement of 0.1% Triton X-100 to remove the nonbinding proteins. Then, the prepared brain lysate was added and incubated for 2 hours at 4°C. After washing four times with the dialysis buffer, the beads resuspended in the loading buffer were boiled at 100°C for 10 min and loaded into an SDS–polyacrylamide gel electrophoresis (PAGE) gel for separation. The lanes in the gel were carefully cut off and digested by trypsin into peptides. After desalting, the samples containing the peptides were analyzed under liquid chromatography–mass spectrometry (Orbitrap Fusion). Last, the data were searched against SwissProt_Mus database by using Mascot to recognize the proteins, which were further analyzed by using the Scaffold software.

Antibodies
The primary antibodies used in this study include rabbit anti-MyoVa (dilute 1:500 for immunofluorescence and 1:1000 for Western blotting; Sigma-Aldrich, HPA001356), mouse anti-MICAL1 (dilute 1:1000 for Western blotting; Sigma-Aldrich, HPA040902), rabbit anti-MICAL1 (dilute 1:200 for immunofluorescence; ProteinTech, 14818-1-AP), mouse anti–β-tubulin (dilute 1:1000 for immunofluorescence; Sangon, D1930693), mouse anti–Aurora B (dilute 1:500 for immunofluorescence; BD, 611082), mouse anti-GAPDH (glyceraldehyde-3-phosphate dehydrogenase) (dilute 1:1000 for Western blotting; Transgene, HT801-01), and mouse anti-Flag (dilute 1:1000 for Western blotting; Sigma-Aldrich, F1804) antibodies. The secondary antibodies used in this study include gat anti-mouse immunoglobulin G (IgG), horseradish peroxidase (HRP)–linked antibody [dilute 1:3000; Cell Signaling Technology

(CST)], goat anti-rabbit IgG, HRP-linked antibody (dilute 1:3000; CST) for Western blotting, and Alexa Fluor 488/594/633–conjugated anti-mouse/rabbit IgG antibody (dilute 1:3000; Invitrogen) for immunofluorescence experiments.

Plasmids
For cell transfection, the full-length mouse MyoVa gene (containing exons D and F) was synthetized after codon optimization by GENEWIZ and introduced into a modified pEGFP-C1 vector. Full-length human MICAL1, Spir1, Spir2, and Rab11a genes were amplified by polymerase chain reaction (PCR) from cDNA as gifts from J. Han's laboratory (Xiamen University) and then inserted to modified pcDNA3.1 fused with an N-terminal 3×Flag tag, modified pEGFP-C1, or pmCherry-C1 vectors. For photoactivation assay, the PAGFP gene was used to replace the eGFP gene in modified pEGFP-C1-MyoVa/Rab11a-Q70L. For protein overexpression in bacteria, MyoVa^{GTD}, MICAL1 with different boundaries, Spir2^{GTBM}, and Rab11a$^{1-177}$ were recombined into modified pET32a or pGEX4T-1 vectors. All the mutants were generated by a QuickChange Site-Directed Mutagenesis kit, and all the plasmids were verified by sequencing.

Cell cultures and transfection
HeLa, Chinese hamster ovary (CHO), and HT1080 cells were cultured in Dulbecco's modified Eagle's medium (Corning) supplemented with 10% fetal bovine serum and penicillin and streptomycin (50 U/ml) in 5% CO_2 condition at 37°C. Transfection was performed using Lipofectamine 3000 (Thermo Fisher Scientific) according to the manufacturer's instructions.

Coimmunoprecipitation experiments
HeLa cells cotransfected with GFP-MyoVa and Flag-MICAL1 or Flag-MICAL1^{ΔGTBM} were harvested after 48 hours and lysed in a buffer containing 20 mM tris (pH7.5), 100 mM KCl, 5 mM $MgCl_2$, 0.5% NP-40, and protease inhibitors. After centrifuge, the supernatants were incubated with anti-Flag antibody for 1 hour, followed by adding Protein A beads for a further 1-hour incubation at 4°C. After washing four times in the lysis buffer, the samples were mixed with the loading buffer, then boiled at 100°C for 10 min, and examined by Western blotting. As a negative control, GFP and Flag-MICAL1 were cotransfected and treated with the same procedures. For the co-IP experiment of the endogenous proteins, HeLa cells without transfection were treated with the similar procedures, except that the supernatants were incubated with anti-MICAL1 antibody or IgG. IgG was used as a negative control.

Immunofluorescence and imaging
HeLa cells were transfected with the plasmids as indicated in figures. After 24 hours, the transfected cells were detached by trypsin treatment and subcultured onto fibronectin-coated coverslips for additional 24 hours. Then, the cells were fixed with 4% paraformaldehyde for 15 min and treated with 0.1% Triton X-100 for another 15 min at room temperature (RT). The fixed cells were stained with the indicated primary antibodies for 1 hour at RT, followed by Alexa Fluor 488/594/633–conjugated anti-mouse/rabbit IgG antibodies for another 1 hour at RT. Cells transfected only with GFP/mCherry-tagged proteins were directly observed without staining after the fixation. For actin analysis experiments, F-actin was stained with SiR-actin dye (Spirochrome). For LatA-induced rescue

experiments, the transfected MICAL1^{KO} cells were treated with 20 nM LatA or dimethyl sulfoxide (DMSO) for 2 hours before the fixation. Confocal images of the cells were acquired with a TCS SP8 microscope (Leica, Germany).

siRNA-mediated knockdown
The siRNAs against human MICAL1 (siMICAL1) with a sequence of 5′-GAGUCCACGUCUCCGAUUU-3′ (41) and the negative control siRNAs (siControl) with a sequence of 5′-UUCUCCGAAC-GUGUCACGU-3′ were synthesized by GenePharma (Shanghai). The siRNAs were dissolved in diethyl pyrocarbonate (DEPC)–H$_2$O and transfected into HeLa cells at a final concentration of 20 nM. After 72-hour transfection, the cells were harvested and lysed in the buffer containing 20 mM tris (pH 7.5), 100 mM KCl, 5 mM MgCl$_2$, 0.5% NP-40, and protease inhibitors. Last, the knockdown efficiency was verified by Western blotting.

CRISPR-Cas9 knockout cell lines
The generations of MICAL1^{KO} and MyoVa^{KO} HeLa cell lines are based on the CRISPR-Cas9–mediated gene disruption system (71). In brief, two guide RNAs (gRNAs) targeting the sequences of 5′-GCGCATGCCCACTTTGAGAG-3′ in MICAL1 and 5′-CACT-TACGAAATCCTGACAT-3′ in MyoVa were designed and inserted into the plasmid pSpCas9(BB)-2A-GFP (PX458, Addgene, #48138). The plasmids with different gRNAs were transfected into HeLa cells, and single GFP-positive cells were sorted into 96-well plates, with each well containing a single colony using a fluorescence-activated cell sorting (FACS) sorter (BD FACSAria III). After cell propagation, MICAL1^{KO} and MyoVa^{KO} HeLa cells were detected and confirmed by sequencing and Western blotting.

Rescue assay
For the rescue in MICAL1^{KD} cells, the HeLa cells were first treated by siMICAL1 for 48 hours and then cotransfected by 20 nM siMICAL1 and siRNA-resistant Flag-tagged MICAL1 or MICAL1$^{\Delta GTBM}$, which were generated by nonsensically mutating 7 base pairs (bp) of siRNA-targeting sequence for an additional 48 hours. For the rescue in MICAL1^{KO} cells, the mCherry/Flag-tagged MICAL1, MICAL1$^{\Delta GTBM}$, or MICAL1-3G3W was directly transfected with or without the mCherry-tagged Rab11-Q70L.

Cytokinesis time measurement
Normal and knockout HeLa cells were cultured in glass dishes and placed in an open chamber, which was kept in 5% CO$_2$ condition at 37°C. Time-lapse sequences were recorded every 5 min for 24 hours using a Nikon living cell system. For rescue experiments, the empty pmCherry-C1, mCherry-MICAL1, or mCherry-MICAL1$^{\Delta GTBM}$ was transfected into MICAL1^{KO} cells and the mCherry-positive cells were sorted into glass dishes after 24-hour transfection with a FACS sorter (BD FACSAria III). After an additional 24-hour culture, the cells with mCherry signals were recorded in real time following the same procedures as described above.

Structured illumination microscopy imaging
Live cell superresolution imaging of normal and MICAL1^{KO} cells expressing mCherry-tagged Rab11-Q70L was performed with an Elyra 7 superresolution microscope (ZEISS, Germany) in lattice structured illumination microscopy (SIM) mode. Cells were maintained in 37°C, 5% CO$_2$ environment during the whole acquisition

process. Raw data were processed with ZEISS ZEN blue software, and then images were analyzed using Imaris software.

Fluorescence recovery after photobleaching
FRAP experiments were performed on an A1R confocal microscope (Nikon, Japan) with a 100× oil immersion objective with a numerical aperture (NA) equal to 1.49. Cells were kept in a humidified condition of 5% CO$_2$ in a 37°C incubation chamber. All cells with the similar protein expression levels were used for analysis. Microtubules were stained with 100 nM SiR-tubulin (Spirochrome) and 10 nM verapamil (Sigma-Aldrich; to inhibit efflux of SiR-tubulin from cells) at least 1 hour before imaging. Following one frame of starting frame recording, photobleaching was performed in the circled region of interest with three iterations of maximum 564-nm excitation laser output with an exposure time of 5 s, and imaging was resumed immediately after and continued for 150 s. Fluorescence measurement was done with background subtraction method. The FRAP curve for each cell under the same condition was normalized for statistical analysis.

Photoactivation
The plasmids containing PAGFP-tagged MyoVa or Rab11a-Q70L were transfected into normal HeLa cells or MICAL1^{KO} cells, respectively. After 24-hour transfection, the cells were incubated with 100 nM SiR-tubulin (Spirochrome) for 1 hour and then kept in a humidified condition of 5% CO$_2$ in a 37°C incubation chamber for imaging using an A1R confocal microscope (Nikon, Japan) with a 100× oil immersion objective, with NA equal to 1.49. Following one frame of starting frame recording, photoactivation was performed in a circled region of interest with a 405-nm excitation laser output and an exposure time of 3 s, and imaging was resumed immediately after and continued for 150 s. The curve for each cell under the same condition was normalized for statistical analysis.

Protein expression and purification
MyoVa^{GTD}, MyoVb^{GTD}, MICAL1 with different boundaries, Spir2^{GTBM}, Rab11a$^{1–177}$, and all the mutants were overexpressed by an induction of 0.2 mM isopropyl-β-D-thiogalactopyranoside (IPTG) at 16°C overnight in BL21(DE3) Escherichia coli cells. The thioredoxin (Trx)–His–fused proteins were purified by using Ni^{2+}–nitrilotriacetic acid (NTA) resin (GE Healthcare), and the GST-fused proteins were purified by gluta-thione Sepharose 4 column (GE Healthcare), followed by size exclusion chromatography (Superdex 200 pg, GE Healthcare) with a buffer of 50 mM tris (pH7.5), 100 mM NaCl, 1 mM DTT, and 1 mM EDTA. For crystallization, Trx-His–fused MyoVa^{GTD} and MICAL1^{GTBM} were treated with 3C protease overnight at 16°C to remove the fused tags and then further purified by a second Ni^{2+}-NTA affinity chromatography, followed by SEC.

GST pull-down and in vitro competition assay
For testing the direct interaction, purified GST or GST-MICAL1 with a concentration of 3.5 μM was first incubated with 40 μl of glutathione Sepharose 4 beads at 4°C for 30 min. After removing the nonbinding proteins, MyoVa^{GTD} was added at a final concentration of 35 μM and the mixture was incubated for another 1 hour at 4°C. After washing four times, the samples were resuspended in protein loading buffer and further analyzed by SDS-PAGE. Conversely, in in vitro competition assay, purified GST-MyoVa^{GTD} was first incubated with glutathione Sepharose 4 beads and then

Spir2^{GTBM} and MICAL1$^{760–917}$ with various concentrations as indicated were added. After washing carefully, the samples were finally analyzed by SDS-PAGE.

Analytical size exclusion chromatography

aSEC was carried out on an ÄKTA pure system (GE Healthcare). Protein samples were prepared with a final concentration of 40 μM and loaded onto a Superdex 200 Increase 10/300 GL column (GE Healthcare), equilibrated with a buffer containing 50 mM tris-HCl (pH 7.5), 100 mM NaCl, 1 mM EDTA, and 1 mM DTT.

Isothermal titration calorimetry

ITC measurements were performed on a VP-ITC Microcal calorimeter (Malvern). The protein samples were prepared with a concentration of 200 to 300 μM in the syringe and 20 μM in the cell. The titration was processed by injecting 10 μl of the sample in the syringe to the cell each time. An interval of 150 s between two injections was set to ensure the curve back to the baseline. The titration data were analyzed using Origin7.0 and fitted by a one-site binding model.

NADPH consumption

The enzymatic activity of MICAL1 was monitored based on the difference of A_{340} (the absorption at the light of 340 nm) between the reduced NADPH and the oxidized NADP$^+$ (72) because MICAL1 is a redox enzyme with a cofactor of NADPH. NADPH was first prepared with a final concentration of 180 μM in the buffer containing 50 mM tris (pH7.5), 100 mM NaCl, 1 mM DTT, and 1 mM EDTA. After pre-equilibration for 10 min, 600 nM protein samples were added to start the reaction and the decreases of A_{340} in the next hour were recorded with an interval of 30 s under an EnSpire plate reader at 25°C to indicate the rate of NADPH consumption.

Crystallization and x-ray data collection

To prepare the complex for crystallization, purified MyoVa^{GTD} and MICAL1^{GTBM} without Trx-His tag were mixed at a ratio of 1:1.2 and incubated on ice for 30 min. The crystals of MyoVa^{GTD} and MICAL1^{GTBM} complex were manually screened by the sitting drop vapor diffusion method at 16°C, based on commercially available sparse matrix screens. Last, the crystals for diffraction were obtained at the condition of 1% (w/v) tryptone, 0.05 M Hepes sodium (pH 7.0), and 20% (w/v) polyethylene glycol 3350. After flash-cooling in liquid nitrogen with crystallization solution containing 30% glycerol as cryo-protection, the crystals were delivered to collect data. Diffraction data were collected at Shanghai Synchrotron Radiation Facility beamline BL19U1 and processed and scaled by the HKL3000 software package (73).

Structure determination and analysis

The initial phase was determined by using molecular replacement method with the apo MyoVa^{GTD} structure [Protein Data Bank (PDB) ID: 3WB8] as a search model, and MICAL1^{GTBM} was further built to obtain the complex structure. The complex structure was manually improved in COOT (74) and then refined against the 1.60-Å resolution dataset by using PHENIX (75), alternatively. In the final stage, an additional TLS (translation, libration and screw-rotation) refinement was performed in PHENIX. The model quality was check by MolProbity (76). The refinement statistics are listed in table S1. All structure figures were prepared using PyMOL (http://www.pymol.org/).

Statistical analysis

All values are displayed with an error bar of SD for at least three independent experiments. Significance was analyzed using an unpaired, two-tailed Student's t test model. In addition, the recognized proteins from mass spectrum were analyzed using the Fisher's exact test model. In all statistical tests, $P > 0.05$ was considered as not significant (NS), while $P < 0.05$ was indicated as "*," $P < 0.01$ as "**," $P < 0.001$ as "***," and $P < 0.0001$ as "****." All the statistical analysis was performed and exported to figures by using the GraphPad Prism 6.0 software.

REFERENCES AND NOTES

1. R. D. Vale, The molecular motor toolbox for intracellular transport. *Cell* **112**, 467–480 (2003).
2. J. L. Ross, M. Y. Ali, D. M. Warshaw, Cargo transport: Molecular motors navigate a complex cytoskeleton. *Curr. Opin. Cell Biol.* **20**, 41–47 (2008).
3. N. Hirokawa, S. Niwa, Y. Tanaka, Molecular motors in neurons: Transport mechanisms and roles in brain function, development, and disease. *Neuron* **68**, 610–638 (2010).
4. M. Schliwa, G. Woehlke, Molecular motors. *Nature* **422**, 759–765 (2003).
5. D. Dwivedi, M. Sharma, Multiple roles, multiple adaptors: Dynein during cell cycle. *Adv. Exp. Med. Biol.* **1112**, 13–30 (2018).
6. S. M. Heissler, J. R. Sellers, Various themes of myosin regulation. *J. Mol. Biol.* **428**, 1927–1946 (2016).
7. M. A. Hartman, D. Finan, S. Sivaramakrishnan, J. A. Spudich, Principles of unconventional myosin function and targeting. *Annu. Rev. Cell Dev. Biol.* **27**, 133–155 (2011).
8. Q. Lu, J. Li, M. Zhang, Cargo recognition and cargo-mediated regulation of unconventional myosins. *Acc. Chem. Res.* **47**, 3061–3070 (2014).
9. K. J. Verhey, J. W. Hammond, Traffic control: Regulation of kinesin motors. *Nat. Rev. Mol. Cell Biol.* **10**, 765–777 (2009).
10. S. L. Reck-Peterson, W. B. Redwine, R. D. Vale, A. P. Carter, The cytoplasmic dynein transport machinery and its many cargoes. *Nat. Rev. Mol. Cell Biol.* **19**, 382–398 (2018).
11. N. Hirokawa, Y. Noda, Y. Tanaka, S. Niwa, Kinesin superfamily motor proteins and intracellular transport. *Nat. Rev. Mol. Cell Biol.* **10**, 682–696 (2009).
12. J. N. Sleigh, A. M. Rossor, A. D. Fellows, A. P. Tosolini, G. Schiavo, Axonal transport and neurological disease. *Nat. Rev. Neurol.* **15**, 691–703 (2019).
13. M. Kneussel, W. Wagner, Myosin motors at neuronal synapses: Drivers of membrane transport and actin dynamics. *Nat. Rev. Neurosci.* **14**, 233–247 (2013).
14. S. L. Reck-Peterson, D. W. Provance Jr., M. S. Mooseker, J. A. Mercer, Class V myosins. *Biochim. Biophys. Acta* **1496**, 36–51 (2000).
15. J. A. Hammer III, J. R. Sellers, Walking to work: Roles for class V myosins as cargo transporters. *Nat. Rev. Mol. Cell Biol.* **13**, 13–26 (2011).
16. J. A. Hammer III, W. Wagner, Functions of class V myosins in neurons. *J. Biol. Chem.* **288**, 28428–28434 (2013).
17. E. Kerkhoff, Actin dynamics at intracellular membranes: The Spir/formin nucleator complex. *Eur. J. Cell Biol.* **90**, 922–925 (2011).
18. J. R. Brown, P. Stafford, G. M. Langford, Short-range axonal/dendritic transport by myosin-V: A model for vesicle delivery to the synapse. *J. Neurobiol.* **58**, 175–188 (2004).
19. J. A. Mercer, P. K. Seperack, M. C. Strobel, N. G. Copeland, N. A. Jenkins, Novel myosin heavy chain encoded by murine *dilute* coat colour locus. *Nature* **349**, 709–713 (1991).
20. M. Van Gele, P. Dynoodt, J. Lambert, Griscelli syndrome: A model system to study vesicular trafficking. *Pigment Cell Melanoma Res.* **22**, 268–282 (2009).
21. K. M. Trybus, Myosin V from head to tail. *Cell. Mol. Life Sci.* **65**, 1378–1389 (2008).
22. J. R. Sellers, C. Veigel, Walking with myosin V. *Curr. Opin. Cell Biol.* **18**, 68–73 (2006).
23. K. A. Taylor, Regulation and recycling of myosin V. *Curr. Opin. Cell Biol.* **19**, 67–74 (2007).
24. L. Cramer, Organelle transport: Dynamic actin tracks for myosin motors. *Curr. Biol.* **18**, R1066–R1068 (2008).
25. I. Semenova, A. Burakov, N. Berardone, I. Zaliapin, B. Slepchenko, T. Svitkina, A. Kashina, V. Rodionov, Actin dynamics is essential for myosin-based transport of membrane organelles. *Curr. Biol.* **18**, 1581–1586 (2008).
26. A. T. Lombardo, S. R. Nelson, G. G. Kennedy, K. M. Trybus, S. Walcott, D. M. Warshaw, Myosin Va transport of liposomes in three-dimensional actin networks is modulated by

actin filament density, position, and polarity. *Proc. Natl. Acad. Sci. U.S.A.* **116**, 8326–8335 (2019).

27. M. Schuh, An actin-dependent mechanism for long-range vesicle transport. *Nat. Cell Biol.* **13**, 1431–1436 (2011).

28. O. Pylypenko, T. Welz, J. Tittel, M. Kollmar, F. Chardon, G. Malherbe, S. Weiss, C. I. Michel, A. Samol-Wolf, A. T. Grasskamp, A. Hume, B. Goud, B. Baron, P. England, M. A. Titus, P. Schwille, T. Weidemann, A. Houdusse, E. Kerkhoff, Coordinated recruitment of Spir actin nucleators and myosin V motors to Rab11 vesicle membranes. *eLife* **5**, e17523 (2016).

29. L. T. Alto, J. R. Terman, MICALs. *Curr. Biol.* **28**, R538–R541 (2018).

30. S. S. Giridharan, S. Caplan, MICAL-family proteins: Complex regulators of the actin cytoskeleton. *Antioxid. Redox Signal.* **20**, 2059–2073 (2014).

31. F. A. Barr, U. Gruneberg, Cytokinesis: Placing and making the final cut. *Cell* **131**, 847–860 (2007).

32. A. B. Fielding, E. Schonteich, J. Matheson, G. Wilson, X. Yu, G. R. Hickson, S. Srivastava, S. A. Baldwin, R. Prekeris, G. W. Gould, Rab11-FIP3 and FIP4 interact with Arf6 and the exocyst to control membrane traffic in cytokinesis. *EMBO J.* **24**, 3389–3399 (2005).

33. G. M. Wilson, A. B. Fielding, G. C. Simon, X. Yu, P. D. Andrews, R. S. Hames, A. M. Frey, A. A. Peden, G. W. Gould, R. Prekeris, The FIP3-Rab11 protein complex regulates recycling endosome targeting to the cleavage furrow during late cytokinesis. *Mol. Biol. Cell* **16**, 849–860 (2005).

34. J. A. Schiel, G. C. Simon, C. Zaharris, J. Weisz, D. Castle, C. C. Wu, R. Prekeris, FIP3-endosome-dependent formation of the secondary ingression mediates ESCRT-III recruitment during cytokinesis. *Nat. Cell Biol.* **14**, 1068–1078 (2012).

35. S. Ohashi, K. Koike, A. Omori, S. Ichinose, S. Ohara, S. Kobayashi, T.-A. Sato, K. Anzai, Identification of mRNA/protein (mRNP) complexes containing Purα, mStaufen, fragile X protein, and myosin Va and their association with rough endoplasmic reticulum equipped with a kinesin motor. *J. Biol. Chem.* **277**, 37804–37810 (2002).

36. A. J. Lindsay, F. Jollivet, C. P. Horgan, A. R. Khan, G. Raposo, M. W. McCaffrey, B. Goud, Identification and characterization of multiple novel Rab–myosin Va interactions. *Mol. Biol. Cell* **24**, 3420–3434 (2013).

37. R.-J. Hung, U. Yazdani, J. Yoon, H. Wu, T. H. Yang, N. Gupta, Z. Y. Huang, W. J. H. van Berkel, J. R. Terman, Mical links semaphorins to F-actin disassembly. *Nature* **463**, 823–827 (2010).

38. R.-J. Hung, C. W. Pak, J. R. Terman, Direct redox regulation of F-actin assembly and disassembly by Mical. *Science* **334**, 1710–1713 (2011).

39. P. Steigemann, D. W. Gerlich, Cytokinetic abscission: Cellular dynamics at the midbody. *Trends Cell Biol.* **19**, 606–616 (2009).

40. C.-K. Hu, M. Coughlin, T. J. Mitchison, Midbody assembly and its regulation during cytokinesis. *Mol. Biol. Cell* **23**, 1024–1034 (2012).

41. S. Frémont, H. Hammich, J. Bai, H. Wioland, K. Klinkert, M. Rocancourt, C. Kikuti, D. Stroebel, G. Romet-Lemonne, O. Pylypenko, A. Houdusse, A. Echard, Oxidation of F-actin controls the terminal steps of cytokinesis. *Nat. Commun.* **8**, 14528 (2017).

42. F. Baluska, D. Menzel, P. W. Barlow, Cytokinesis in plant and animal cells: Endosomes 'shut the door'. *Dev. Biol.* **294**, 1–10 (2006).

43. S. Frémont, A. Echard, Membrane traffic in the late steps of cytokinesis. *Curr. Biol.* **28**, R458–R470 (2018).

44. O. Ullrich, S. Reinsch, S. Urbé, M. Zerial, R. G. Parton, Rab11 regulates recycling through the pericentriolar recycling endosome. *J. Cell Biol.* **135**, 913–924 (1996).

45. A. Rai, A. Oprisko, J. Campos, Y. Fu, T. Friese, A. Itzen, R. S. Goody, E. M. Gazdag, M. P. Müller, bMERB domains are bivalent Rab8 family effectors evolved by gene duplication. *eLife* **5**, e18675 (2016).

46. Z. Wei, X. Liu, C. Yu, M. Zhang, Structural basis of cargo recognitions for class V myosins. *Proc. Natl. Acad. Sci. U.S.A.* **110**, 11314–11319 (2013).

47. E. Kerkhoff, Cellular functions of the Spir actin-nucleation factors. *Trends Cell Biol.* **16**, 477–483 (2006).

48. J. R. Terman, T. Mao, R. J. Pasterkamp, H.-H. Yu, A. L. Kolodkin, MICALs, a family of conserved flavoprotein oxidoreductases, function in plexin-mediated axonal repulsion. *Cell* **109**, 887–900 (2002).

49. S. S. Giridharan, J. L. Rohn, N. Naslavsky, S. Caplan, Differential regulation of actin microfilaments by human MICAL proteins. *J. Cell Sci.* **125**, 614–624 (2012).

50. K. Thirumurugan, T. Sakamoto, J. A. Hammer III, J. R. Sellers, P. J. Knight, The cargo-binding domain regulates structure and activity of myosin 5. *Nature* **442**, 212–215 (2006).

51. J. Liu, D. W. Taylor, E. B. Krementsova, K. M. Trybus, K. A. Taylor, Three-dimensional structure of the myosin V inhibited state by cryoelectron tomography. *Nature* **442**, 208–211 (2006).

52. X. Wu, T. Sakamoto, F. Zhang, J. R. Sellers, J. A. Hammer III, In vitro reconstitution of a transport complex containing Rab27a, melanophilin and myosin Va. *FEBS Lett.* **580**, 5863–5868 (2006).

53. X.-D. Li, R. Ikebe, M. Ikebe, Activation of myosin Va function by melanophilin, a specific docking partner of myosin Va. *J. Biol. Chem.* **280**, 17815–17822 (2005).

54. K. W. Donovan, A. Bretscher, Myosin-V is activated by binding secretory cargo and released in coordination with Rab/exocyst function. *Dev. Cell* **23**, 769–781 (2012).

55. M. E. Quinlan, J. E. Heuser, E. Kerkhoff, R. D. Mullins, *Drosophila* Spire is an actin nucleation factor. *Nature* **433**, 382–388 (2005).

56. D. B. Bekker-Jensen, C. D. Kelstrup, T. S. Batth, S. C. Larsen, C. Haldrup, J. B. Bramsen, K. D. Sørensen, S. Høyer, T. F. Ørntoft, C. L. Andersen, M. L. Nielsen, J. V. Olsen, An optimized shotgun strategy for the rapid generation of comprehensive human proteomes. *Cell Syst.* **4**, 587–599.e4 (2017).

57. N. Nagaraj, J. R. Wisniewski, T. Geiger, J. Cox, M. Kircher, J. Kelso, S. Pääbo, M. Mann, Deep proteome and transcriptome mapping of a human cancer cell line. *Mol. Syst. Biol.* **7**, 548 (2011).

58. E. E. Grintsevich, H. G. Yesilyurt, S. K. Rich, R.-J. Hung, J. R. Terman, E. Reisler, F-actin dismantling through a redox-driven synergy between Mical and cofilin. *Nat. Cell Biol.* **18**, 876–885 (2016).

59. E. Y. Van Battum, R.-A. Gunput, S. Lemstra, E. J. Groen, K. L. Yu, Y. Adolfs, Y. Zhou, C. C. Hoogenraad, Y. Yoshida, M. Schachner, A. Akhmanova, R. J. Pasterkamp, The intracellular redox protein MICAL-1 regulates the development of hippocampal mossy fibre connections. *Nat. Commun.* **5**, 4317 (2014).

60. Q. Liu, F. Liu, K. L. Yu, R. Tas, I. Grigoriev, S. Remmelzwaal, A. Serra-Marques, L. C. Kapitein, A. J. Heck, A. Akhmanova, MICAL3 flavoprotein monooxygenase forms a complex with centralspindlin and regulates cytokinesis. *J. Biol. Chem.* **291**, 20617–20629 (2016).

61. R. O'Hagan, M. Silva, K. C. Q. Nguyen, Y. Zhang, S. Bellotti, Y. H. Ramadan, D. H. Hall, M. M. Barr, Glutamylation regulates transport, specializes function, and sculpts the structure of cilia. *Curr. Biol.* **27**, 3430–3441.e6 (2017).

62. F. T. Salles, R. C. Merritt Jr., U. Manor, G. W. Dougherty, A. D. Sousa, J. E. Moore, C. M. Yengo, A. C. Dosé, B. Kachar, Myosin IIIa boosts elongation of stereocilia by transporting espin 1 to the plus ends of actin filaments. *Nat. Cell Biol.* **11**, 443–450 (2009).

63. U. Manor, A. Disanza, M. H. Grati, L. Andrade, H. Lin, P. P. Di Fiore, G. Scita, B. Kachar, Regulation of stereocilia length by myosin XVa and whirlin depends on the actin-regulatory protein Eps8. *Curr. Biol.* **21**, 167–172 (2011).

64. R. C. Merritt, U. Manor, F. T. Salles, M. Grati, A. C. Dose, W. C. Unrath, O. A. Quintero, C. M. Yengo, B. Kachar, Myosin IIIB uses an actin-binding motif in its espin-1 cargo to reach the tips of actin protrusions. *Curr. Biol.* **22**, 320–325 (2012).

65. A. K. Rzadzinska, E. M. Nevalainen, H. M. Prosser, P. Lappalainen, K. P. Steel, MyosinVIIa interacts with Twinfilin-2 at the tips of mechanosensory stereocilia in the inner ear. *PLOS ONE* **4**, e7097 (2009).

66. M. C. Seabra, E. Coudrier, Rab GTPases and myosin motors in organelle motility. *Traffic* **5**, 393–399 (2004).

67. L. Guillaud, R. Wong, N. Hirokawa, Disruption of KIF17–Mint1 interaction by CaMKII-dependent phosphorylation: A molecular model of kinesin–cargo release. *Nat. Cell Biol.* **10**, 19–29 (2008).

68. R. G. Yau, S. Wong, L. S. Weisman, Spatial regulation of organelle release from myosin V transport by p21-activated kinases. *J. Cell Biol.* **216**, 1557–1566 (2017).

69. R. G. Yau, Y. Peng, R. R. Valiathan, S. R. Birkeland, T. E. Wilson, L. S. Weisman, Release from myosin V via regulated recruitment of an E3 ubiquitin ligase controls organelle localization. *Dev. Cell* **28**, 520–533 (2014).

70. R. L. Karcher, J. T. Roland, F. Zappacosta, M. J. Huddleston, R. S. Annan, S. A. Carr, V. I. Gelfand, Cell cycle regulation of myosin-V by calcium/calmodulin-dependent protein kinase II. *Science* **293**, 1317–1320 (2001).

71. F. A. Ran, P. D. Hsu, J. Wright, V. Agarwala, D. A. Scott, F. Zhang, Genome engineering using the CRISPR-Cas9 system. *Nat. Protoc.* **8**, 2281–2308 (2013).

72. H. Wu, H. G. Yesilyurt, J. Yoon, J. R. Terman, The MICALs are a family of F-actin dismantling oxidoreductases conserved from drosophila to humans. *Sci. Rep.* **8**, 937 (2018).

73. W. Minor, M. Cymborowski, Z. Otwinowski, M. Chruszcz, *HKL-3000*: The integration of data reduction and structure solution—From diffraction images to an initial model in minutes. *Acta Crystallogr. D Biol. Crystallogr.* **62**, 859–866 (2006).

74. P. Emsley, B. Lohkamp, W. G. Scott, K. Cowtan, Features and development of *Coot*. *Acta Crystallogr. D Biol. Crystallogr.* **66**, 486–501 (2010).

75. P. D. Adams, P. V. Afonine, G. Bunkóczi, V. B. Chen, I. W. Davis, N. Echols, J. J. Headd, L.-W. Hung, G. J. Kapral, R. W. Grosse-Kunstleve, A. J. McCoy, N. W. Moriarty, R. Oeffner, R. J. Read, D. C. Richardson, J. S. Richardson, T. C. Terwilliger, P. H. Zwart, *PHENIX*: A comprehensive Python-based system for macromolecular structure solution. *Acta Crystallogr. D Biol. Crystallogr.* **66**, 213–221 (2010).

76. V. B. Chen, W. B. Arendall III, J. J. Headd, D. A. Keedy, R. M. Immormino, G. J. Kapral, L. W. Murray, J. S. Richardson, D. C. Richardson, *MolProbity*: All-atom structure validation for macromolecular crystallography. *Acta Crystallogr. D Biol. Crystallogr.* **66**, 12–21 (2010).

Citation: F. Niu, K. Sun, W. Wei, C. Yu, Z. Wei, F-actin disassembly factor MICAL1 binding to Myosin Va mediates cargo unloading during cytokinesis. *Sci. Adv.* **6**, eabb1307 (2020).